Preprints of the 21st IFAC World Congress (Virtual)
Berlin, Germany, July 12-17, 2020

Minimizing observation spillover for pose control of elastic bodies using optimal sensor placement

Kevin Schmidt * **Neşe Inan** * **Johannes Schüle** *
Michael Böhm * **Alexander Kharitonov** ** **Oliver Sawodny** *

* *Institute for System Dynamics, University of Stuttgart, Germany*
(e-mail: schmidt@isys.uni-stuttgart.de)
** *Faculty of Mechanical Engineering, University of Applied Sciences Würzburg-Schweinfurt, Germany*

Abstract: The impact of elastic modes limits the performance of position control of elastic bodies in a significant way. Local dampers are a typical way to suppress this issue, but lead to non-proportional damping and complex oscillation modes with varying nodal lines. To this end, the placement of the sensors is of major importance in high-precision applications. In this contribution, we present an optimal sensor placement algorithm which uses Gramian-based observability measures to overcome this issue. Singular sensing configurations with respect to the pose are avoided by considering the mappings' local invertibility explicitly. Furthermore, we are in the position to cope with the highly relevant issue of constrained installation space and to handle complex 2D and 3D geometries by using model order reduction techniques. By means of an illustrative example, the significantly reduced influence of the elastic deformations on the controller is demonstrated at last.

Keywords: high-precision control, optimal sensor placement, observation spillover

1. INTRODUCTION

The presence of elastic modes is a ubiquitous issue when controlling the pose of mechatronic systems and arising in various applications, see Munnig Schmidt et al. (2014); Korkmaz (2011); Schmidt et al. (2019). The problem can be handled by using notch filters as in Hoogendijk et al. (2014), however at the expense of the maximum bandwidth of the closed loop system. Secondly, structural damping is supplemented by local damping (such as tuned mass dampers, see Vervoordeldonk et al. (2006)), in order to suppress the influence of elastic oscillation modes. The latter solution evokes complex-valued modes which are characterized by spatially-varying nodes and extrema as demonstratively visualized in Fig. 1. Hence, intuitive sensor placement strategies, e.g. placing sensors in the modes' nodal lines, are not applicable anymore. The issue of constrained installation space further complicates the derivation of sensing configurations with minimal observation spillover. Hence, we propose an optimization-based approach for deriving a valid sensing configuration. The latter one consists of at least six pairs of measurement points and directions, which are necessary to estimate the rigid-body pose in a 3D context. Besides the minimization of the observation spillover, the local invertibility of this mapping is crucial since it determines the amplification of sensor noise.

The *contribution* of this work is the development of an optimal sensor placement algorithm which uses Gramian-based measures for the control spillover and the invertibility of the pose reconstruction at the same time. Constraints on the sensor configuration arising from space restrictions and demands on minimal distances between the sensing points can be incorporated into the optimization scheme. As a starting point, we model the bodies' motion by means of partial differential equations (PDEs). According to Craig and Bampton (1968), the overall motion is split up into an elastic and a rigid-body movement, as the observation spillover only concerns the elastic component. Based on this representation, a modal analysis of the elastic motion is the next step to a lumped design model. This article is organized as follows: We first characterize the problem and the objective from a technical point of view in section 2. Subsequently, section 3 deals with the optimization approach including the model order reduction and the determination of valid sensor candidates. We close the paper by providing an illustrative 2D example in section 4 in order to demonstrate the most important parts of the algorithm.

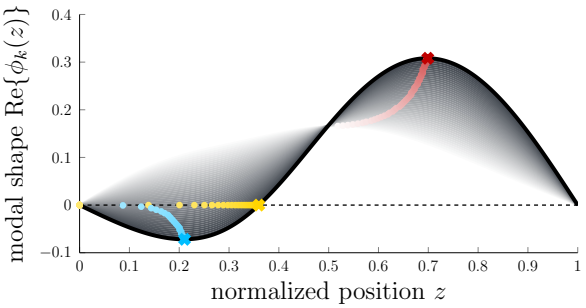

Fig. 1. Complex-valued oscillation mode. Due to non-proportional damping, the loci of extrema (red and blue) and nodes (yellow) are phase-dependent.

2. MODELING AND PROBLEM DESCRIPTION

Before considering the sensor placement algorithm in more detail, a rigorous problem description is presented. We first introduce the elastic bodies' governing equations of motion in subsection 2.1, and focus on representation of the measured outputs subsequently. The contribution and the objective are then summarized from a technical point of view in subsection 2.3.

2.1 Dynamic Model Equations

The overall objective is to control the rigid body pose $\mathscr{P}$ of a body $\mathcal{B} \subset \mathbb{R}^n$, at a particular point of interest with high precision despite of transient elastic deformations being present. We define the pose as the equilibrium configuration of the body $\mathcal{B}$ for constant external forces. Without any loss of generality, the bodies' center of gravity $\boldsymbol{x}_c$ is chosen. The respective pose

$$\mathscr{P} = \{\boldsymbol{x}_\mathrm{c}, \boldsymbol{\theta}_\mathrm{c}\} \in \mathbb{R}^N \quad \text{where } N = \frac{n(n+1)}{2} \tag{1}$$

comprises $\dim \boldsymbol{x}_c = n$ translations and $\dim \boldsymbol{\theta}_c = n(n-1)/2$ rotations with respect to the undeformed body. Further, let $\boldsymbol{n}^{\partial\mathcal{B}}(\boldsymbol{z},t)$ be the outer normal vector of the bodies' surface $\partial\mathcal{B}$ and $\boldsymbol{x}(\boldsymbol{z},t)$ the deflection field for each location $\boldsymbol{z} \in \mathcal{B}$ at a specific time $t \geq 0$.

Equations of Motion. Since only small variations of the initial pose $\mathscr{P}_0$ are relevant, the assumption of small deflections $\boldsymbol{x}(\boldsymbol{z},t)$ with respect to an initial state $\boldsymbol{x}^0(\boldsymbol{z}) \in \mathcal{B}$ is natural. For this, the linear equations of motion

$$\mathcal{M}\frac{\partial^2 \boldsymbol{x}}{\partial t^2}(\boldsymbol{z},t) + \mathcal{D}\frac{\partial \boldsymbol{x}}{\partial t}(\boldsymbol{z},t) + \mathcal{K}\boldsymbol{x}(\boldsymbol{z},t) = \boldsymbol{0} \tag{2}$$

can be used for all $\boldsymbol{z} \in \mathcal{B}$ and all $t > 0$. Without any loss of generality, we assume the initial conditions $\boldsymbol{x}(\boldsymbol{z},0) = \boldsymbol{z}$ and $\partial\boldsymbol{x}(\boldsymbol{z},0)/\partial t = \boldsymbol{0}$ for all $\boldsymbol{z} \in \mathcal{B}$. Here, $\mathcal{M}$, $\mathcal{D}$, and $\mathcal{K}$ denote the mass, damping, and stiffness operators. The present contribution focuses on, but is not limited to, non-proportional damping sometimes referred as non-Rayleigh damping. In this case, the Rayleigh assumption does not hold and the damping operator cannot be expressed by means of the mass and stiffness operators, i.e. $\mathcal{D} \notin \mathrm{span}(\mathcal{M},\mathcal{K})$. As an example for this problem class is the linear elastic body with an Navier-Cauchy stiffness operator

$$\mathcal{K}\boldsymbol{x} = -G\left[\Delta\boldsymbol{x} + \frac{1}{1-2\nu}\nabla\left(\nabla\cdot\boldsymbol{x}\right)\right], \tag{3}$$

see Ehlers and Bluhm (2013), an isotropic density $\mathcal{M} = \rho = const.$ and spatially varying damping $\mathcal{D} = d(\boldsymbol{z})$.

Boundary Conditions and Actuation. Since the particular actuation principle is not of interest for the sensor placement scheme, we assume N points of the bodies' boundary $\partial\mathcal{B}$ to be position controlled, i.e. $\boldsymbol{\alpha}_j^\intercal \boldsymbol{x}(\boldsymbol{a}_j,t) = u_j(t)$, with $\boldsymbol{\alpha}_j$ and $\boldsymbol{a}_j$ being the actuation direction and the actuation point of the input u_j respectively. For the sake of simplicity, we assume decoupled actuator dynamics regarding a desired control $\boldsymbol{u}_\mathrm{d}$ of the form

$$\dot{\boldsymbol{\mu}} = \boldsymbol{A}_\mathrm{u}\boldsymbol{\mu} + \boldsymbol{B}_\mathrm{u}\boldsymbol{u}_\mathrm{d}, \qquad \boldsymbol{u} = \boldsymbol{C}_\mathrm{u}\boldsymbol{\mu} \tag{4}$$

with $\boldsymbol{C}_\mathrm{u}\boldsymbol{A}_\mathrm{u}^{-1}\boldsymbol{B}_\mathrm{u} + \boldsymbol{I} = \boldsymbol{0}$, relative degrees $r_j > 2$, and Hurwitz dynamics with sufficiently large bandwidth $\min\|\lambda(\boldsymbol{A}_\mathrm{u})\| \geq 2\pi f_{\mathrm{bw,u}}$. All other points $\partial\mathcal{B} \setminus \boldsymbol{a}_j$ are assumed be free of tension or external forces. According to Cauchy's theorem, we receive the Neumann boundary condition $\boldsymbol{\sigma}(\boldsymbol{z},t)\boldsymbol{n}^{\partial\mathcal{B}}(z,t) = \boldsymbol{0}$ in dependence of the stress tensor $\boldsymbol{\sigma}$, see Ehlers and Bluhm (2013).

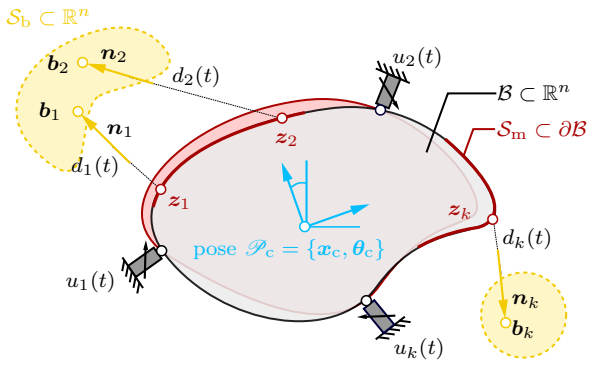

Fig. 2. Problem description. The actual configuration of the elastic body $\mathcal{B}$, actuated by N inputs $u_k(t)$, is measured by K distance measurements $d_k(t)$ between the respective mounting points $\boldsymbol{z}_k$ on the bodies surface and the base points $\boldsymbol{b}_k$.

Rigid-Body and Elastic Deformation. The decomposition of bodies' displacement in rigid-body motion and elastic modes is a crucial notion for the desired spillover reduction by optimal sensor placement. Thus, we use the decomposition

$$\boldsymbol{x}(\boldsymbol{z},t) = \boldsymbol{x}^\mathrm{s}(\boldsymbol{z},t) + \boldsymbol{x}^\mathrm{e}(\boldsymbol{z},t), \tag{5}$$

where $\boldsymbol{x}^\mathrm{s}$ is referred to as the rigid-body deflection. It contains the information of the pose $\mathscr{P}$ to be controlled or observed, respectively. The rigid-body motion is an algebraic function of the inputs, i.e. $\boldsymbol{x}^\mathrm{s}(\boldsymbol{u})$, and defined by the equilibrium solution of PDE (2) with corresponding inhomogeneous boundary conditions:

$$\boldsymbol{x}^\mathrm{s}(\boldsymbol{u}): \quad \mathcal{K}\boldsymbol{x}^\mathrm{s}(\boldsymbol{z},t) = \boldsymbol{0}, \quad \boldsymbol{\alpha}_j^\intercal \boldsymbol{x}^\mathrm{s}(\boldsymbol{a}_j,t) = u_j(t). \tag{6}$$

In related research, this representation is denoted as 'rigid-body modes' and is associated with the zero-eigenvalues of the overall system Craig and Bampton (1968). Even for complex geometries, the rigid-body modes can be computed by means of numerical methods such as finite element analysis, see Panzer et al. (2009); Siebelts et al. (2018) for instance.

The remaining movement $\boldsymbol{x}^\mathrm{e}$ represents the transient elastic deformations, whose impact on the measured output shall be minimal. By combining (2) and (6) we receive

$$\mathcal{M}\frac{\partial^2 \boldsymbol{x}^\mathrm{e}}{\partial t^2} + \mathcal{D}\frac{\partial \boldsymbol{x}^\mathrm{e}}{\partial t} + \mathcal{K}\boldsymbol{x}^\mathrm{e} = -\mathcal{M}\boldsymbol{x}^\mathrm{s}(\ddot{\boldsymbol{u}}) - \mathcal{D}\boldsymbol{x}^\mathrm{s}(\dot{\boldsymbol{u}}) \tag{7}$$

with homogenized boundary conditions $\boldsymbol{\alpha}_j^\intercal \boldsymbol{x}^\mathrm{e}(\boldsymbol{a}_j,t) = 0$. In comparison to the original system, the elastic deformations asymptotically vanish for $\boldsymbol{u} = const.$ having a stable spectrum for physically meaningful operators.

2.2 Sensor Configuration

Measured Outputs. Since the objective of the paper is to determine an optimal sensor configuration, the notion of sensing configurations is crucial. As illustrated in Fig. 2, we assume that the measurement system features K distance measurements. Many optical measurement systems such as optical linear encoders or LIDAR sensors can be named

as examples. In more detail, each sensor features a base point $\boldsymbol{b}_k$, located at a fixed external point, as well as a mounting point $\boldsymbol{z}_k$, located on the bodies' surface. The particular sensor signal is distance $d_k(t)$ between those points, which depends on the local deflection $\boldsymbol{x}(\boldsymbol{z}_k, t)$ and is given by $d_k(t) = \|\boldsymbol{b}_k - (\boldsymbol{z}_k + \boldsymbol{x}(\boldsymbol{z}_k, t))\|$. Since small deflections are considered, we take the Taylor expansion of the above equation with respect to the undeformed configuration into account and receive the relation

$$d_k(t) = \underbrace{\|\boldsymbol{b}_k - \boldsymbol{z}_k\|}_{d_k^0} + \underbrace{\frac{\partial d_k}{\partial \boldsymbol{x}}\bigg|_{\boldsymbol{x}=\boldsymbol{0}}^{\intercal}}_{\boldsymbol{n}_k^{\intercal}} \boldsymbol{x}(\boldsymbol{z}_k, t) + \mathcal{O}(\|\boldsymbol{x}\|^2), \quad (8)$$

with normalized sensing direction between the base and the mounting point

$$\boldsymbol{n}_k = \frac{\boldsymbol{b}_k - \boldsymbol{z}_k}{\|\boldsymbol{b}_k - \boldsymbol{z}_k\|} = \frac{\boldsymbol{b}_k - \boldsymbol{z}_k}{d_k^0}. \quad (9)$$

Thus, we end up with the linearized sensing equation

$$y_k(t) \triangleq d_k(t) - d_k^0 = \boldsymbol{n}_k^{\intercal} \boldsymbol{x}(\boldsymbol{z}_k, t), \quad (10)$$

which describes the change of distance with respect to the initial configuration. Since the output equation directly depends on the mounting point $\boldsymbol{z}_k$ and the sensing direction $\boldsymbol{n}_k$, it is more convenient to use the tupel $(\boldsymbol{z}_k, \boldsymbol{n}_k)$ to parametrize a particular sensor than the base and the corresponding mounting point $(\boldsymbol{z}_k, \boldsymbol{b}_k)$. All in all, a whole sensing configuration S consists of $K \geq N$ sensors

$$S = \left\{ (\boldsymbol{z}_k, \boldsymbol{n}_k) \;\middle|\; k = 1, ..., K \right\} \quad (11)$$

which lead to the output vector $\boldsymbol{y}(t) \in \mathbb{R}^K$.

Sensor Constraints. The definition and consideration of constraints is an essential part of the algorithm, since the issue of limited construction space is ubiquitous. More specifically, we consider two kind of constraints in this paper: While the first one defines sets of valid positions for each individual base and mounting points, the second one addresses the overall sensor configuration.

As sketched in Fig. 2, we define two sets to describe the valid sensor locations. All sensor base points need to be located in the so-called sensor base set $\boldsymbol{b}_k \in \mathcal{S}_\mathrm{b} \subset \mathbb{R}^n \setminus \mathcal{B}$, which is a subset of $\mathbb{R}^n$ and does not include the elastic body. A similar set is defined for the mounting points $\boldsymbol{z}_k \in \mathcal{S}_\mathrm{m} \subset \partial\mathcal{B}$ which restricts the allowed sensor locations on the surface of the body. Moreover, mentioned sets comprise several subsets, which do not have to be connected necessarily. Note that this kind of constraint can be considered a priori, allowing only white-listed candidates $(\boldsymbol{z}_k, \boldsymbol{n}_k)$ for the optimization.

Given the whole sensing configuration S defined in (11), we further define the minimal distance of the involved mounting points

$$\Delta z^-(S) = \min_{\substack{1 \leq k,m \leq K \\ k \neq m}} \|\boldsymbol{z}_m - \boldsymbol{z}_k\| \quad (12)$$

in order to account for the required sensor mounting space within the optimization. Analogously, a similar condition for the base points can be derived. Using (9), we obtain

$$\Delta b^-(S) = \min_{\substack{1 \leq k,m \leq K \\ k \neq m}} \left\| \boldsymbol{z}_m + \boldsymbol{n}_m d_m^0 - \boldsymbol{z}_k - \boldsymbol{n}_k d_k^0 \right\|. \quad (13)$$

In contrast to the white-listing of the individual points and directions, distance constraints of the form $\Delta b^-(S) \geq \Delta p_\mathrm{min}$ cannot be guaranteed beforehand, but have to be considered as inequality constraints.

2.3 Contribution and Objectives

The overall objective of this paper is the pose control of elastic bodies. In this framework, the error between a desired pose $\mathscr{P}_\mathrm{d} = \tilde{\boldsymbol{u}}_\mathrm{d}$ and the measured pose $\mathscr{P} = \tilde{\boldsymbol{y}}$ is fed back into the system through a control transfer matrix. The conversion of a desired pose to an actor configuration $\boldsymbol{u} = \boldsymbol{a}(\tilde{\boldsymbol{u}})$, and of measured outputs to the actual pose $\tilde{\boldsymbol{y}} = \boldsymbol{m}^{-1}(\boldsymbol{y})$ is essential. This paper focuses on the latter aspect only. Given an elastic body described by (2) and measured outputs (10), the contribution is to determine an optimal sensing configuration $S^\star$, featuring valid sensor mounting points $\boldsymbol{z}_k \in \mathcal{S}_\mathrm{m}$ and directions $\boldsymbol{n}_k$, which

- allows a well-defined reconstruction of the pose $\mathscr{P}$ according to the rigid-body movement $\boldsymbol{x}^\mathrm{s}$, see (6),
- minimizes the observation spillover induced by elastic deformations $\boldsymbol{x}^\mathrm{e}$ defined by (7),
- corresponds to valid sensor base points $\boldsymbol{b}_k \in \mathcal{S}_\mathrm{b}$, and
- satisfies the minimum distances constraints introduced in (12), (13).

3. OPTIMAL SENSOR PLACEMENT ALGORITHM

This section describes a solution to the multi-objective optimization problem stated above, starting with introducing the cost function in section 3.1. As a further prerequisite, the derivation of a lumped design model and other preprocessing steps are stated subsequently. At last, the solution of the resulting (mixed) integer programming problem is focused in section 3.3.

3.1 Optimization Problem

In order to determine an optimum for the multi-objective problem stated in part 2.3, we use the scalarized problem

$$\begin{aligned}
\min_S \quad & J(S) = w_1 \frac{\mathrm{tr}\boldsymbol{Q}(S) - \mathrm{tr}\boldsymbol{Q}^\star}{\mathrm{tr}\boldsymbol{Q}^0 - \mathrm{tr}\boldsymbol{Q}^\star} + w_2 \frac{\mu(S) - \mu^\star}{\mu^0 - \mu^\star} && \text{(14a)} \\
\text{s.t.} \quad & \boldsymbol{z}_k \in \mathcal{S}_\mathrm{m} && \text{(14b)} \\
& \boldsymbol{z}_k + d_k^0 \boldsymbol{n}_k \in \mathcal{S}_\mathrm{b} && \text{(14c)} \\
& \Delta z_\mathrm{min} \leq \Delta z^-(S) && \text{(14d)} \\
& \Delta b_\mathrm{min} \geq \Delta b^-(S). && \text{(14e)}
\end{aligned}$$

The cost function comprises two components, which are explained in the subsequent paragraphs in more detail. While the trace of the design model's observability Gramian $\boldsymbol{Q}$ is used to minimize the observation spillover, an invertibility index μ of the measurement Jacobian is used as a metric of the pose reconstruction. Both objectives can hardly be compared since their values differ by orders of magnitude. As a consequence, we normalize both components with an affine mapping taking the cost of an initial solution S_0 as well as the individual optima $\mathrm{tr}\boldsymbol{Q}^\star$ and $\mu^\star$ into account.

Metric for Observation Spillover. Based on a lumped state space representation of the form $\dot{\boldsymbol{x}} = \boldsymbol{A}\boldsymbol{x} + \boldsymbol{B}\boldsymbol{u}$ with output $\boldsymbol{y} = \boldsymbol{C}\boldsymbol{x} + \boldsymbol{D}\boldsymbol{u}$, the Gramian observability matrix

$$\boldsymbol{Q} = \int_0^\infty \exp\left(\boldsymbol{A}^\intercal \tau\right) \boldsymbol{C}^\intercal \boldsymbol{C} \exp\left(\boldsymbol{A}\tau\right) \mathrm{d}\tau \quad (15)$$

can be used as an adequate metric for the observation spillover. Since the eigenvalues of $\boldsymbol{Q}$ are related to

the observability of the respective states, minimizing the trace tr$\boldsymbol{Q}$ is equivalent to minimizing the overall impact of the state on the output $\boldsymbol{y}$. Further details on how to construct a lumped state-space is given in the subsequent subsection 3.2.

Measurement Jacobian. The key idea of the second metric is to exploit properties of the mapping $\boldsymbol{d} = \boldsymbol{m}(\mathscr{P})$, whose components describe how a certain output varies when changing the pose. For the desired pose reconstruction, an inverse mapping has to be derived. In the general case, a closed-form expression for $\boldsymbol{m}^{-1}$ can hardly be deduced, especially for redundant sensors configurations with $K > N$. For each sensor y_k, a row $\widetilde{\boldsymbol{m}}_j^\intercal$ of the measurement Jacobian

$$\widetilde{\boldsymbol{M}} = \left.\frac{\partial \boldsymbol{m}}{\partial \mathscr{P}}\right|_{\mathscr{P}_0} = \begin{bmatrix} \widetilde{\boldsymbol{m}}_1^\intercal \\ \vdots \\ \widetilde{\boldsymbol{m}}_K^\intercal \end{bmatrix} \in \mathbb{R}^{K\times N}, \tag{16}$$

with $\boldsymbol{y} = \widetilde{\boldsymbol{M}}[\mathscr{P} - \mathscr{P}_0]$. We can now define the second component μ of the cost function for any specific sensing configuration S:

$$\mu(S) \triangleq \left\|\widetilde{\boldsymbol{M}}(S)\right\|_{\mathrm{F}} \left\|\widetilde{\boldsymbol{M}}^{+}(S)\right\|_{\mathrm{F}} \in [1, \infty), \tag{17}$$

which uses the Moore-Penrose Pseudo-inverse $(\cdot)^+$ and the Frobenius matrix norm $\|(\cdot)\|_{\mathrm{F}}$. As $\mu(S)$ tends to infinity for singular constructions, (17) is an adequate metric for the reconstructablity of the rigid-body pose. A second argument for choosing the ansatz (17) as a metric is its relation to the amplification of disturbances $\boldsymbol{y} + \delta\boldsymbol{y}$. The deviation of the solution $\mathscr{P} + \delta\mathscr{P}$ can be bounded by

$$\frac{\|\delta\mathscr{P}\|}{\|\mathscr{P}\|} \leq \mu(S) \cdot \frac{\|\delta \boldsymbol{y}\|}{\|\boldsymbol{y}\|}. \tag{18}$$

using $\|\delta\mathscr{P}\| \leq \|\widetilde{\boldsymbol{M}}^{+}\|_{\mathrm{F}} \cdot \|\delta\boldsymbol{y}\|$ and definition (17). The disturbances $\delta\boldsymbol{y}$ may represent the influence of the elastic modes for instance. Note that a Jacobian $\tilde{\boldsymbol{A}}$ for transforming the actuator coordinates $\boldsymbol{u}$ to pose coordinates $\tilde{\boldsymbol{u}}$ can be derived analogously.

3.2 Preprocessing and Initialization

Valid sensors and individual constraints. Before focusing on the discretization of the equations of motion, a set of valid sensor candidates $(\boldsymbol{z}_k, \boldsymbol{n}_k)$ satisfying the individual sensor constraints (14b)–(14c) can be derived by geometric arguments. As a prerequisite, we assume that a spatial discretization of the body $\mathcal{B}$ by means of a grid G, as well as the sets $\mathcal{S}_{\mathrm{m}}$ and $\mathcal{S}_{\mathrm{b}}$ are given. Starting with the evaluation of the individual sensor mounting constraints, we determine all $\bar{k} = 1, \ldots, \bar{K}$ surfacial grid points $\boldsymbol{z}_{\bar{k}}^{\mathrm{v}} \in \mathcal{S}_{\mathrm{m}}$ in the mounting set. To figure out the valid sensing directions, a discretized n-sphere of possible directions $\boldsymbol{n}_{\tilde{k}}$ with $\tilde{k} = 1, \ldots, \tilde{K}$ is created – e.g. by spherical Fibonacci mappings, Keinert et al. (2015). As shown in Fig. 3, we evaluate the following conditions for every pair $(\boldsymbol{z}_{\bar{k}}^{\mathrm{v}}, \boldsymbol{n}_{\tilde{k}})$, to determine if the angle between the measurement direction and the local normal vector is smaller than $\pi/2$ and if there exists a valid base point in $\mathcal{S}_{\mathrm{b}}$:

$$\boldsymbol{n}_{\tilde{k}}^\intercal \boldsymbol{n}^{\partial\mathcal{B}}(\boldsymbol{z}_{\bar{k}}^{\mathrm{v}}) \geq 0, \qquad \exists d_{\tilde{k}}^0 > 0: \quad \boldsymbol{z}_{\bar{k}}^{\mathrm{v}} + d_{\tilde{k}}^0 \boldsymbol{n}_{\tilde{k}} \in \mathcal{S}_{\mathrm{b}} \tag{19}$$

Note that for determining a sufficient total number K_{tot} of sensor candidates $(\boldsymbol{z}_k, \boldsymbol{n}_k)$ discretization $\bar{K}$ needs to be chosen comparably high if small solid angles are valid. To prepare the computation of (17), we compute each $\widetilde{\boldsymbol{m}}_k^\intercal$.

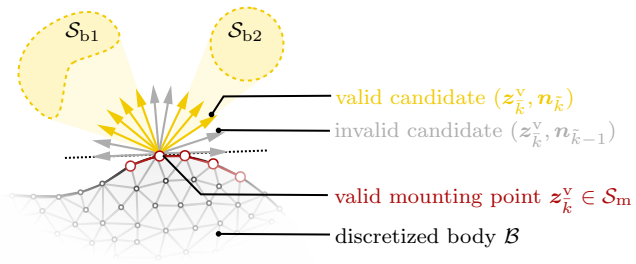

Fig. 3. Determination of valid sensor candidates.

Discretization and modal truncation. The first step towards an adequate design model is to derive a lumped model for the elastic PDE (7) and the overall PDE (2) respectively. After a spatial discretization scheme on the grid G, such as the finite element or finite differences method, has been applied, a model order reduction is necessary. We obtain approximations for the stiffness and damping operators of the form

$$\mathcal{K}\boldsymbol{x}|_{\boldsymbol{z}\in G} \approx \boldsymbol{K}\boldsymbol{\xi} = \boldsymbol{K}^{\mathrm{e}}\boldsymbol{\xi} + \boldsymbol{K}^{\mathrm{s}}\boldsymbol{u} \tag{20}$$

$$\mathcal{D}\left.\frac{\partial \boldsymbol{x}}{\partial t}\right|_{\boldsymbol{z}\in G} \approx \boldsymbol{D}\dot{\boldsymbol{\xi}} = \boldsymbol{D}^{\mathrm{e}}\dot{\boldsymbol{\xi}} + \boldsymbol{D}^{\mathrm{s}}\dot{\boldsymbol{u}}, \tag{21}$$

where $\boldsymbol{\xi}(t)$ is the high-dimensional discretized vector of deflections. Furthermore, the matrices $\boldsymbol{K}^{\mathrm{s}}$ and $\boldsymbol{D}^{\mathrm{s}}$ represent the influence of the boundary conditions. As a consequence, the elastic parts $\boldsymbol{K}^{\mathrm{e}}$ and $\boldsymbol{D}^{\mathrm{e}}$ remain for $\boldsymbol{u} = \boldsymbol{0}$. In the discretized setting, the non-proportional damping leads to $\boldsymbol{D}^{\mathrm{e}} \neq \alpha\boldsymbol{M} + \beta\boldsymbol{K}^{\mathrm{e}}$ for any $\alpha, \beta \in \mathbb{R}$, where $\boldsymbol{M}$ denotes the mass matrix.
With this notation, the approximation $\boldsymbol{\xi}^{\mathrm{s}}(\boldsymbol{u})$ of the rigid-body deflection $\boldsymbol{x}^{\mathrm{s}}(\boldsymbol{u})$ from (6) reads as

$$\boldsymbol{\xi}^{\mathrm{s}}(\boldsymbol{u}) = -(\boldsymbol{K}^{\mathrm{e}})^{-1}\boldsymbol{K}^{\mathrm{s}}\boldsymbol{u} \triangleq \boldsymbol{\phi}^{\mathrm{s}}\boldsymbol{u}. \tag{22}$$

On the other hand, we obtain the discretized elastic motion

$$\boldsymbol{M}\ddot{\boldsymbol{\xi}}^{\mathrm{e}} + \boldsymbol{D}^{\mathrm{e}}\dot{\boldsymbol{\xi}}^{\mathrm{e}} + \boldsymbol{K}^{\mathrm{e}}\boldsymbol{\xi}^{\mathrm{e}} = \boldsymbol{F}\boldsymbol{\mu} \tag{23}$$

with $\boldsymbol{F} = -\boldsymbol{M}\boldsymbol{\phi}^{\mathrm{s}}\boldsymbol{C}_{\mathrm{u}}\boldsymbol{A}_{\mathrm{u}}^2 - \boldsymbol{D}^{\mathrm{e}}\boldsymbol{\phi}^{\mathrm{s}}\boldsymbol{C}_{\mathrm{u}}\boldsymbol{A}_{\mathrm{u}}$ by evaluating PDE (7) with (4),(20), and (21). The respective complex-valued elastic modes $\boldsymbol{\Psi} = [\boldsymbol{\psi}_1, \boldsymbol{\psi}_2, \ldots]$ with eigenvalues $\boldsymbol{\Lambda} = \mathrm{diag}\{\lambda_1, \lambda_2, \ldots\}$ are the solution to the generalized eigenvalue problem

$$\begin{bmatrix} \boldsymbol{D}^{\mathrm{e}} & \boldsymbol{M} \\ \boldsymbol{M} & \boldsymbol{0} \end{bmatrix} \begin{bmatrix} \boldsymbol{\Psi} \\ \boldsymbol{\Psi}\boldsymbol{\Lambda} \end{bmatrix} \begin{bmatrix} \boldsymbol{\Lambda} & \boldsymbol{0} \\ \boldsymbol{0} & \boldsymbol{\Lambda} \end{bmatrix} = \begin{bmatrix} -\boldsymbol{K}^{\mathrm{e}} & \boldsymbol{0} \\ \boldsymbol{0} & \boldsymbol{M} \end{bmatrix} \begin{bmatrix} \boldsymbol{\Psi} \\ \boldsymbol{\Psi}\boldsymbol{\Lambda} \end{bmatrix}. \tag{24}$$

Next, a normalization $\boldsymbol{\Psi}^0 = \boldsymbol{\Psi}\boldsymbol{\Gamma}^{-\frac{1}{2}}$ with respect to the augmented mass matrix can be performed, where

$$\boldsymbol{\Gamma} = \boldsymbol{\Psi}^\intercal\boldsymbol{D}^{\mathrm{e}}\boldsymbol{\Psi} + \boldsymbol{\Psi}^\intercal\boldsymbol{M}\boldsymbol{\Psi}\boldsymbol{\Lambda} + \boldsymbol{\Gamma}\boldsymbol{\Psi}^\intercal\boldsymbol{M}\boldsymbol{\Lambda}. \tag{25}$$

By choosing only the first $m = 1, \ldots, M$ pairs of complex-conjugated modes, sorted w.r.t. the absolute value of

$$\lambda_m = -\zeta_m\omega_m \pm j\omega_m\sqrt{1-\zeta_m^2}, \tag{26}$$

we achieve a modal truncation. For the sake of simplicity, we assume no critically damped modes to be present. The remaining M pairs of complex-conjugated modes and eigenvalues are rearranged as follows:

$$\hat{\boldsymbol{\Lambda}} = \mathrm{diag}\{\lambda_1, \bar{\lambda}_1, \ldots, \lambda_M, \bar{\lambda}_M\} \in \mathbb{C}^{2M\times 2M}, \tag{27a}$$

$$\hat{\boldsymbol{\Psi}} = [\boldsymbol{\psi}_1, \bar{\boldsymbol{\psi}}_1, \ldots, \boldsymbol{\psi}_M, \bar{\boldsymbol{\psi}}_M] \in \mathbb{C}^{nN_G\times 2M}. \tag{27b}$$

In order to end up with M real-valued 2×2 blocks of integrator chains, we define the transformation

$$\boldsymbol{T}_m = \begin{bmatrix} 0 & 1 \\ \omega_m\sqrt{1-\zeta_m^2} & -\omega_m\zeta_m \end{bmatrix} \begin{bmatrix} 1 & 1 \\ -j & j \end{bmatrix} \tag{28}$$

for each pair to build up the block diagonal $\boldsymbol{T} = \mathbb{C}^{2M\times 2M}$ with the real-valued transformed modes $\boldsymbol{\Phi} = \hat{\boldsymbol{\Psi}}\boldsymbol{T}^{-1}$. One advantage of transform (28) is that the algorithm is not limited to measuring distances, but can be augmented to velocities. In the present case, we receive one row

$$y_k(t) = \sum_{m=1}^{M} [\boldsymbol{n}_k^\intercal \boldsymbol{\phi}_m(\boldsymbol{z}_k), \quad 0] \begin{bmatrix} q_m(t) \\ \dot{q}_m(t) \end{bmatrix} \triangleq \boldsymbol{c}_k^\intercal \boldsymbol{\Phi} \boldsymbol{q}^{\mathrm{e}}(t) \tag{29}$$

of the output matrix $\boldsymbol{C} \in \mathbb{R}^{K\times 2M}$ w.r.t. the reduced generalized coordinates $\boldsymbol{\xi}(t) \approx \boldsymbol{\Phi}\boldsymbol{q}^{\mathrm{e}}(t)$. Combining, (4), (22)–(23), and (27a)–(29) the reduced-order design model for overall deformation is given by

$$\frac{\mathrm{d}}{\mathrm{d}t}\begin{bmatrix} \boldsymbol{q}^{\mathrm{e}} \\ \boldsymbol{\mu} \end{bmatrix} = \begin{bmatrix} \boldsymbol{T}\hat{\boldsymbol{\Lambda}}\boldsymbol{T}^{-1} & \boldsymbol{\Phi}^\intercal \boldsymbol{F}\tilde{\boldsymbol{A}}\boldsymbol{C}_{\mathrm{u}} \\ \boldsymbol{0} & \boldsymbol{A}_{\mathrm{u}} \end{bmatrix} \begin{bmatrix} \boldsymbol{q}^{\mathrm{e}} \\ \boldsymbol{\mu} \end{bmatrix} + \begin{bmatrix} \boldsymbol{0} \\ \boldsymbol{B}_{\mathrm{u}} \end{bmatrix} \tilde{\boldsymbol{u}}_{\mathrm{d}} \tag{30a}$$

$$\tilde{\boldsymbol{y}} = \widetilde{\boldsymbol{M}}^{+}\boldsymbol{C}\left(\boldsymbol{\Phi}\boldsymbol{q}^{\mathrm{e}} + \boldsymbol{\phi}^{\mathrm{s}}\tilde{\boldsymbol{A}}\tilde{\boldsymbol{u}}_{\mathrm{d}}\right) \tag{30b}$$

Finally, the observability of the pair $(\boldsymbol{T}\hat{\boldsymbol{\Lambda}}\boldsymbol{T}^{-1}, \widetilde{\boldsymbol{M}}^{+}\boldsymbol{C})$ determines the amount of spillover on the measured pose $\tilde{\boldsymbol{y}}$. The corresponding Gramian $\boldsymbol{Q}$ can be computed with the Lyapunov equation

$$[\boldsymbol{T}\hat{\boldsymbol{\Lambda}}\boldsymbol{T}^{-1}]^\intercal \boldsymbol{Q} + \boldsymbol{Q}^\intercal \boldsymbol{T}\hat{\boldsymbol{\Lambda}}\boldsymbol{T}^{-1} + \boldsymbol{C}^\intercal [\widetilde{\boldsymbol{M}}^{+}]^\intercal \widetilde{\boldsymbol{M}}^{+}\boldsymbol{C} = \boldsymbol{0}. \tag{31}$$

3.3 Computation of Optimal Solutions

With the preprocessing steps described above, the original optimization problem (14), could be reduced to a (mixed) integer nonlinear programming (MINLP) type. In addition, the determined K_{tot} sensing candidates $(\boldsymbol{z}_k, \boldsymbol{n}_k)$ already satisfy the individual constraints (14b)–(14c). For determining the optimal choice, we define the Boolean vector $\boldsymbol{s} \in \{0,1\}^{K_{\mathrm{tot}}}$ which represents which of the candidates are chosen. With the 1-norm $K = \|\boldsymbol{s}\|_1$ the number of chosen sensors can be evaluated easily. Thus, by fixing the valid maximum number of sensors, i.e. $\|\boldsymbol{s}\|_1 = N$, redundancy is not allowed. The remaining computational effort for an evaluation of the scalarized cost (3.1) is comparably low: Solely precalculated matrices need to be arranged, the Frobenius norm norms of the measurement Jacobian have to be computed according to (17), and the Lyapunov equation (31) has to be solved. The resulting optimization problem

$$\min_{\boldsymbol{s}\in\{0,1\}^{K_{\mathrm{tot}}}} \quad w_1 \frac{\mathrm{tr}\boldsymbol{Q}(\boldsymbol{s}) - \mathrm{tr}\boldsymbol{Q}^\star}{\mathrm{tr}\boldsymbol{Q}^0 - \mathrm{tr}\boldsymbol{Q}^\star} + w_2 \frac{\mu(\boldsymbol{s}) - \mu^\star}{\mu^0 - \mu^\star} \tag{32a}$$

$$\text{s.t.} \quad N \le \|\boldsymbol{s}\|_1 \le K_{\max} \tag{32b}$$

$$\Delta z_{\min} \le \Delta z^-(\boldsymbol{s}) \tag{32c}$$

$$\Delta b_{\min} \le \Delta b^-(\boldsymbol{s}) \tag{32d}$$

can be solved by using conventional MINLP-solvers. The provided solutions of the subsequent section were computed with a NSGAII differential evolution strategy, see Qin et al. (2008). Note that a combinatorial solution is not expedient: If it is desired to pick $6 \le K \le 12$ sensors in a 3D setup out of $K_{\mathrm{tot}} = 2000$ candidates, one obtains more than $8.2 \cdot 10^{30}$ permutations.

4. ILLUSTRATIVE EXAMPLE

In order to demonstrate the performance of the proposed sensor placement scheme, a simple example of form (2) is chosen such that the crucial parts of the algorithm can be illustrated more clearly. In more detail, the deflection

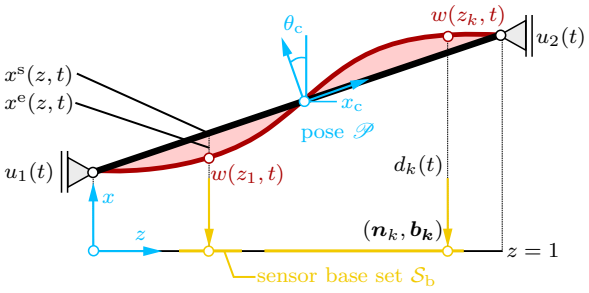

Fig. 4. Sketch of the illustrative example. The deflection $w(z_k,t)$ at two points $z_k \in \mathcal{S}_{\mathrm{m}}$ in the valid sensor mounting set is obtained by measuring the distances $d_k(t)$ of the respective sensor points $\boldsymbol{b}_k \in \mathcal{S}_{\mathrm{b}}$.

$\boldsymbol{x} = [x(\boldsymbol{z},t), 0] \in \mathbb{R}^2$ of a normalized Euler-Bernoulli beam with non-proportional and Kelvin-Voigt damping in a 2D plane $\boldsymbol{z} \in \mathbb{R}^2$ is considered throughout this section. As the second part of the deflection vanishes, a scalar PDE on $(z,t) \in (0,1)\times\mathbb{R}^+$ remains:

$$\rho h \frac{\partial^2 x}{\partial t^2} + d(z)\frac{\partial x}{\partial t} + \frac{d_0}{L^4}\frac{\partial^5 x}{\partial z^4 \partial t} + \frac{EI}{L^4}\frac{\partial^4 x}{\partial z^4} = 0 \tag{33}$$

According to the notation in (2) this example corresponds to the operators $\mathcal{M} = \rho h = const.$, $\mathcal{D} = d(z) + d_0\partial_z^4$, and $\mathcal{K} = EI\partial_z^4$. We assume a step-like spatially variant damping function

$$d(z) = d_1 \sigma(z - z_{\mathrm{d},1})\sigma(z_{\mathrm{d},2} - z) \tag{34}$$

to model a tuned mass damper with $z_{\mathrm{d},1} = 0.244$, $z_{\mathrm{d},2} = 0.468$. The resulting modes $\psi_m(z)$ are complex-valued, as there exists no Rayleigh-representation of the damping operator. As further illustrated in Fig. 4, we use the boundary actuation

$$x(0,t) = u_1(t) \qquad \left.\frac{\partial^2 x(z,t)}{\partial z^2}\right|_{z\in\{0,1\}} = 0 \tag{35}$$

$$x(1,t) = u_2(t). \tag{36}$$

and conclude that there remains only a single translational degree of freedom for center of gravity $\boldsymbol{x}_{\mathrm{c}} = [1/2, x_c]$. Consequently, the pose is considered as $\mathscr{P} = \{x_c, \theta_c\}$ in the following. Since the elastic motion of the chosen example is 1D, the first component of the measurement directions can be neglected without any loss of information. We hence restrict all measurement directions to $\boldsymbol{n} = [0,1]^\intercal$, consider the whole body as valid mounting set, and use solely the base set $\mathcal{S}_{\mathrm{b}}$ for the remaining z_k-positions as

$$[z_k, 0] \in \mathcal{S}_{\mathrm{b}} = \{\boldsymbol{b}\in\mathbb{R}^2 | b_1 \in [0.15, 0.85]\setminus(0.35, 0.40), b_2 = 0\}$$

with the output equations $y_k(t) = w(z_k,t)$.

Modal decomposition and rigid-body modes. In accordance with section 3.2, the separation of elastic deformations and rigid-body modes is the first step of the algorithm. It is straightforward to obtain the stationary deflection in closed-form and the respective rigid-body modes:

$$x^{\mathrm{s}}(z,t) = u_1(t) + z[u_2(t) - u_1(t)] = [1-z,\ z]\,\boldsymbol{u}(t). \tag{37}$$

By inserting the above equation in (33) we obtain the dynamics of the infinite-dimensional elastic deflection

$$\rho h \frac{\partial^2 x^{\mathrm{e}}}{\partial t^2} + d(z)\frac{\partial x^{\mathrm{e}}}{\partial t} + \frac{d_0}{L^4}\frac{\partial^5 x^{\mathrm{e}}}{\partial z^4 \partial t} + \frac{EI}{L^4}\frac{\partial^4 x^{\mathrm{e}}}{\partial z^4} = -\rho h \ddot{u}_1 + \\ + \rho h z[\ddot{u}_1 - \ddot{u}_2] + z d(z)[\dot{u}_1 - \dot{u}_2] - d(z)\dot{u}_1 \tag{38}$$

for $z \in (0,1)$ which comes with homogenized boundary conditions $x^{\mathrm{e}}(0,t) = x^{\mathrm{e}}(1,t) = 0$. Even for the simple

case with piece-wise constant damping, there is no closed-form solution for the complex eigenform $\psi_m(z) \in \mathbb{C}$ to the best of the authors' knowledge. As motivated in the introduction (see. Fig. 1), the resulting oscillation modes

$$x_k(z,t) \propto A(z)\sin(\gamma(z)+\omega_k t) \tag{39}$$

have spatially varying amplitude $A(z)$ *and* phase $\gamma(z)$ profiles due to inseparable spatial and temporal operators – leading to spatially varying loci of some maxima, minima and nodes. Some profiles (39) are provided in Fig. 5 for selected modes and where computed by solving the generalized eigenvalue problem (24) after a spatial discretization by means of finite differences with 300 grid points.

Sensor and Actuator Map. The example allows deriving a closed-form representation $x^{\mathscr{P}}(z) = \tan(\theta_c)[z-\frac{1}{2}]+x_c$ of (37) in dependance of the pose, leading to the Jacobian:

$$\tilde{\boldsymbol{u}}(t) = \frac{1}{2}\frac{\partial}{\partial \mathscr{P}}\begin{bmatrix}2x_c-\tan\theta_c\\ 2x_c+\tan\theta_c\end{bmatrix}\Bigg|_{\mathscr{P}_0}\boldsymbol{u}(t) = \tilde{\boldsymbol{A}}\boldsymbol{u}(t) \tag{40}$$

The components of the sensor mapping $m_k(z_k) = x^{\mathscr{P}}(z_k)$ with the Jacobian $\widetilde{\boldsymbol{m}}_k^\intercal = [1, (z_k-\frac{1}{2})(\tan^2\theta_{c,d}+1)]$ follow analogously, see (16). Moreover, for $N=K=2$ sensors and $\theta_{c,d}=0$, we obtain the result

$$\mu(\boldsymbol{z}) = \frac{10z_1^2+2z_2^2-8z_1z_2-6z_1+2z_2+5}{2(z_2-z_1)}. \tag{41}$$

for (17), with the properties $\mu\to\infty$ if $z_1\to z_2$, and $\partial\mu/\partial(z_2-z_1)>0$ for all sensor base positions $0\le z_1<z_2\le 1$. This circumstance implies, that a minimum μ corresponds to a maximum sensor base distance. The same analysis for $N>K$ implies that minimizing μ is equivalent to equally distribute the sensors (and directions in 3D).

Optimal sensor placement. The evaluation of the sensor constraint on the spatial grid yields $K_{\text{tot}}=195$ valid candidates $\boldsymbol{z}_k^{\text{v}}$ and thus $\boldsymbol{s}\in\{0,1\}^{195}$. We choose a minimal distance of $\Delta z_{\min}=0.1$, placed no more than $K_{\max}=10$ sensors and considered $M=25$ elastic modes. Starting with an initial guess $\boldsymbol{z}^0=[0.33,\ 0.67]^\intercal$, the optimal positions for the individual optimization are

$$\boldsymbol{z}(\boldsymbol{s}^\star_{\text{tr}\boldsymbol{Q}}) = [0.24,\ \ 0.56,\ \ 0.75]^\intercal \tag{42a}$$
$$\boldsymbol{z}(\boldsymbol{s}^\star_{\mu}) = [0.15,\ \ 0.85]^\intercal \tag{42b}$$

Note that (42b) uses the maximum allowed distance, as implied from (41). The multi-objective solution of (32) with the weights $w_1=2w_2$ yields the optimal sensing positions $\boldsymbol{z}(\boldsymbol{s}^\star)=[0.15,\ \ 0.79]^\intercal$. The result reduces the individual cost to 34% (tr$\boldsymbol{Q}$) and 77% (μ) of the initial cost.

In order to depict the improvement in terms of observability, the maximum magnitudes $M_{\max}(\omega_k)$ of the transfer matrix $\tilde{\boldsymbol{y}}^{\text{e}}(j\omega)=\boldsymbol{G}(j\omega)\tilde{\boldsymbol{u}}(j\omega)$ from inputs to the elastic components of the outputs at the modal resonant frequencies ω_k are considered. According to Tab. 1, the suppression of the shown modes is significantly improved – especially the amplification of the first mode with $M^0_{\max}(\omega_k)>0\,\text{dB}$ is handled better.

Table 1. Maximum Magnitudes for selected resonant frequencies ω_k

magnitude	initial guess $\boldsymbol{s}^0$	optimal solution $\boldsymbol{s}^\star$
$M_{\max}(\omega_1)$	$+1.07\,\text{dB}$	$-5.06\,\text{dB}$
$M_{\max}(\omega_2)$	$-2.91\,\text{dB}$	$-9.26\,\text{dB}$
$M_{\max}(\omega_3)$	$-17.3\,\text{dB}$	$-24.4\,\text{dB}$

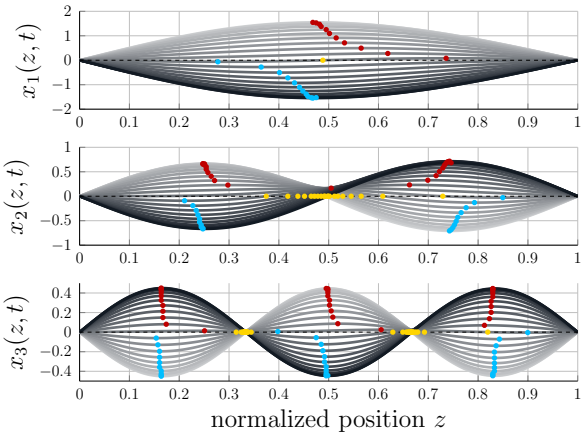

Fig. 5. Complex oscillation modes for $k=1,2,3$ of the example PDE (38) with phase-dependent loci of maxima (red), minima (blue) and nodes (yellow).

5. CONCLUSION

As elastic deformations limit the performance of high-precision pose controllers, passive dampers are typically used to enforce given damping requirements. However, the resulting equations are governed by non-proportional damping and the resulting observation spillover limits the performance of the overall control loop. Furthermore, limitations of the installation space make an intuitive choice of the sensing positions impossible. As a solution, we introduced an optimal sensor placement algorithm in order to minimize the impact of the elastic modes on the measured outputs. The multi-objective optimization considers Gramian-based measures and the invertibility of pose reconstruction at the same time and is capable of evaluating redundant sensor configurations.

REFERENCES

Craig, R. and Bampton, M. (1968). Coupling of substructures for dynamic analyses. *Aiaa Journal*.

Ehlers, W. and Bluhm, J. (2013). *Porous Media: Theory, experiments and Numerical Applications*. Springer.

Hoogendijk, R., Heertjes, M., Van de Molengraft, M., and Steinbuch, M. (2014). Directional notch filters for motion control of flexible structures. *Mechatronics*.

Keinert, B., Innmann, N., Sänger, N., and Stamminger, N. (2015). Spherical fibonacci mapping. *ACM Transactions on Graphics*, 34.

Korkmaz, S. (2011). A review of active structural control: challenges for engineering informatics. *Computers & Structures*.

Munnig Schmidt, R., Schitter, G., and Rankers, A. (2014). *The Design of High Performance Mechatronics-: High-Tech Functionality by Multidisciplinary System Integration*. Ios Press.

Panzer, H., Hubele, J., Eid, R., and Lohmann, B. (2009). Generating a parametric finite element model of a 3d cantilever timoshenko beam using matlab. Technical report, Chair of Automatic Control.

Qin, A.K., Huang, V.L., and Suganthan, P.N. (2008). Differential evolution algorithm with strategy adaptation for global numerical optimization. *IEEE transactions on evolutionary computation*.

Schmidt, K., Raisch, A., and Sawodny, O. (2019). Designing pneumatically actuated deformable mirrors: control of circular plates with varying thickness. In *American Control Conference*.

Siebelts, D., Kater, A., and Meurer, T. (2018). Modeling and motion planning for an artificial fishtail. *IFAC-PapersOnLine*.

Vervoordeldonk, M., van Eijk, J., and Roozen, N. (2006). Active structural damping in high-precision equipment. In *ISMA*.